Materials Advances

ROYAL SOCIETY OF CHEMISTRY

PAPER

View Article Online
View Journal | View Issue

Cite this: *Mater. Adv.*, 2022, 3, 5947

Metal ion-intercalated layered hydrogen titanate nanotubes: synthesis, characterization and their use in ultrafast and enhanced removal of hazardous contaminant fluoride from water†

Anjana Biswas and Prathibha C.*

Titanate nanotubes are a versatile class of materials with a myriad of potential applications. In the present work, hydrogen titanate nanotubes (HTNTs) were functionalized with metal ions, Ce(III), Ca(II), Cu(II), Mg(II), Ni(II) and Ag(I) to enhance the surface properties. The layered crystallographic structure of the HTNTs aided in the efficient intercalation of the metal ions. The developed metal ion-incorporated titanate nanotubes (MTNTs) were thoroughly characterized and studied to understand their physicochemical properties. The phase and structure of the materials were studied through X-ray diffraction, Raman and FTIR spectroscopy. The hollow nanotubular morphology and the incorporation of metal ions into the MTNTs were confirmed by the TEM images and EDS analysis, respectively. The highly porous nature and high surface area of the materials were elucidated by the analysis of BET-based nitrogen adsorption and desorption isotherms. The surface area values were in the range of 165–247 $m^2\ g^{-1}$. The optical properties were analysed using UV-VIS spectroscopy and the band gaps were found to be in the range of 2.57–3.21 eV. The materials were further applied towards adsorption of fluoride ions from water. The effects of various parameters on the adsorption were studied in batch mode. The Langmuir adsorption capacities of the MTNTs were in the range of 98.35–183.34 mg g^{-1}, in the order CaTNTs > AgTNTs > CuTNTs > CeTNTs > NiTNTs > MgTNTs > HTNTs. In addition to their high efficiencies, the MTNTs also showed ultrafast removal of fluoride from water within just 1 min of contact time. The metal ion incorporation into the HTNT structure therefore made them superior fluoride adsorbents compared to the parent material.

Received 20th April 2022,
Accepted 1st June 2022

DOI: 10.1039/d2ma00434h

rsc.li/materials-advances

1. Introduction

Functionalization of materials to develop new products is attracting attention in various fields of application. Doping, intercalation and impregnation are some of the pathways for functionalization and development of new materials. It is essential to understand the structure of the parent material in order to understand the ease and effectiveness of the functionalization process.

Protonated titanate nanotubes, with $H_2Ti_3O_7$ phase, are versatile materials that have been used as potential materials for various applications including electrode materials for batteries and supercapacitors, electronics, water splitting, photocatalysis, dye degradation and so on.[1,2] These can be easily synthesized *via* a hydrothermal route and their morphology can be varied easily, making them further important materials to study the material properties as a function of their morphology. The layered crystallographic structure of the monoclinic titanates ($H_2Ti_3O_7$) is an exciting feature that allows the researchers to functionalize them effectively as per the requirement. Therefore, a lot of research has been focused towards this direction of functionalization of hydrogen titanate nanotubes (HTNTs) with metallic and non-metallic groups, which could enhance and tune various surface properties.[3–6] In the present work, the authors have functionalized HTNTs to employ them as efficient adsorbents for the removal of fluoride from water.

The presence of ionic contaminants in water is a problem that the world is facing today. Fluoride contamination of water is one such global issue affecting 260 million people of the world population from 25 countries, India being one of them.[1] The presence of fluoride in potable water in concentrations above 1.5 mg L^{-1} is considered harmful by the World Health Organization (WHO), whereas the Bureau of Indian Standards (BIS) has set the safe limit to be 1 mg L^{-1}.[7,8] Excess fluoride in

Department of Physics, Sri Sathya Sai Institute of Higher Learning, Anantapur Campus, Andhra Pradesh-515001, India. E-mail: cprathibha@sssihl.edu.in, mailprathinow@gmail.com; Tel: +91-9490362024

† Electronic supplementary information (ESI) available. See DOI: https://doi.org/10.1039/d2ma00434h

water causes skeletal and dental fluorosis, impairs the kidneys, causes Alzheimer's disease affecting the brain, affects the gastrointestinal tract, impacts the metabolic activities and can lead to cancer.[9,10] Therefore, it is necessary to remove the excess fluoride from water, in order to render it safe. Among the various reported techniques, adsorption is considered to be the most efficient technique due to its ease of operation, low cost and efficiency.[11,12]

The quest for efficient fluoride adsorbents has resulted in the development of various adsorbents.[11,13–15] Among the materials reported in the literature, nanomaterials have attracted special attention due to their small size and high surface to volume ratio. The bulk materials either have low adsorption efficiency or have very slow adsorption kinetics making them unsuitable for real time applications. The nano adsorbents, on the other hand, show rapid adsorption kinetics with good efficiency and are therefore potential adsorbents for real-time fluoride adsorption.[1,16]

In our previous work, we investigated the efficiency of an interesting material, HTNTs, and presented a detailed report on their fluoride adsorption properties.[10] In order to further enhance the adsorption capacity and to make them effective for both low and high fluoride concentrations, HTNTs were functionalized with metal ions. As mentioned, their structure allows the intercalation of metal ions in the interlayer spaces of the HTNTs leading to an increased number of active adsorption sites. In addition, the inclusion of metal cations would result in increased positive charge density on the material. It was therefore hypothesized that these factors together would result in improved adsorption capacity in the metal ion-functionalized titanate nanotubes (MTNTs).

In the current work, the authors have functionalized HTNTs with six different metal ions: Ce(III), Ca(II), Mg(II), Ni(II), Cu(II) and Ag(I). These metal ions were chosen based on their electronegativity and reported affinity for fluoride ions.[11,17–19] This is a first-hand report on the systematic functionalization of titanate nanotubes with six metal ions along with the exhaustive analysis and simultaneous comparison of their phase, structure, surface and optical properties and evaluation of their applicability for fluoride adsorption. The structural properties of each of the developed materials were thoroughly characterized with the help of XRD, EDS, TEM, BET, UV-VIS, Raman and FTIR. The as synthesized nanomaterials, MTNTs, were examined for treatment of fluoride contaminated water *via* an adsorption process. This was carried out *via* a batch adsorption process to investigate the impact of pH, contact time, initial concentration and dosage on the process of adsorption using each of the MTNTs. These materials have been proved to be excellent adsorbents with high adsorption capacity and rapid kinetics, which is discussed in the subsequent sections.

2. Materials and methods

2.1 Materials

Analytical grade chemicals were utilized in various experiments reported in this research work. Anatase titanium dioxide (TiO_2), calcium nitrate tetrahydrate ($Ca(NO_3)_2{\cdot}4H_2O$) and cerium nitrate hexahydrate ($Ce(NO_3)_3{\cdot}6H_2O$) were purchased from Alfa Aesar. Copper nitrate trihydrate ($Cu(NO_3)_2{\cdot}3H_2O$), nickel nitrate hexahydrate ($Ni(NO_3)_2{\cdot}6H_2O$), magnesium nitrate ($Mg(NO_3)_2$), silver nitrate ($AgNO_3{\cdot}H_2O$) and sodium hydroxide pellets (NaOH) were purchased from Merck. Absolute ethanol was purchased from Haymann. Anhydrous sodium fluoride (NaF) was purchased from Sigma Aldrich. Total ionic strength adjustment buffer, TISAB-II, was purchased from ThermoScientific, USA. Double distilled water was used for various experiments reported in this work.

2.2 Development of the materials

The alkaline hydrothermal method was used to synthesize titanate nanotubes. The procedure is reported in our previous work.[10] Briefly, 3 g of anatase TiO_2 was uniformly dispersed in 10 M NaOH, which was subjected to hydrothermal treatment at 130 °C for 20 h. The product was recovered by filtration and washing. The bright white residue was thoroughly washed with double distilled water, 0.1 M HCl and ethanol after which it was dried at 80 °C overnight. The synthesis procedure follows the reaction: $2NaOH + 3TiO_2 \rightarrow Na_2Ti_3O_7 \downarrow + H_2O$. The washing procedure leads to ion exchange and yields $H_2Ti_3O_7$: $Na_2Ti_3O_7 + 2HCl \rightarrow H_2Ti_3O_7 + 2NaCl$.

In step 2 of the synthesis procedure, the as synthesized HTNTs were functionalized with metal ions. 250 mg of the bright white HTNT powder was added to 100 mL of 0.1 mol L^{-1} solutions of the metal ion precursors, namely, cerium nitrate, copper nitrate, calcium nitrate, magnesium nitrate, nickel nitrate and silver nitrate for functionalization of the HTNTs with Ce(III), Cu(II), Ca(II), Mg(II), Ni(II) and Ag(I), respectively. This reaction mixture was maintained at 75 °C under continuous magnetic stirring for a period of 20 h. After the specified period, the product was filtered and washed with double distilled water to remove any unreacted metal ions. The products obtained were air dried at 80 °C overnight. The dried products were labelled as M-TNTs, where M = Ce(III), Cu(II), Mg(II), Ni(II) and Ag(I). A schematic of the synthesis procedure is given in Fig. 1.

2.3 Characterization facilities used

The phases of the as synthesized materials were identified using a PANalytical X'Pert Pro system with copper K_α as the source (λ = 1.5406 Å), and a room temperature X-ray diffractometer. The structure of the materials was further elucidated with the help of a Thermo Scientific Raman microscope, which used a 780 nm laser as an excitation source. The elemental analysis of the MTNTs and HTNTs was carried out using a RUSA SEM – energy dispersive X-ray spectroscopy facility. The morphology, size and selective aperture electron diffraction (SAED) patterns of the synthesized nanomaterials were confirmed using a HR-TEM 200 kV JEM-2100 Plus transmission electron microscope. The optical properties were analysed using a LAMBDA 1050 – PerkinElmer UV-VIS-NIR spectrophotometer. The functional groups of the materials were identified using an Agilent Cary 630 Fourier transform infrared spectrometer. The surface areas and the pore size of the materials were studied using a

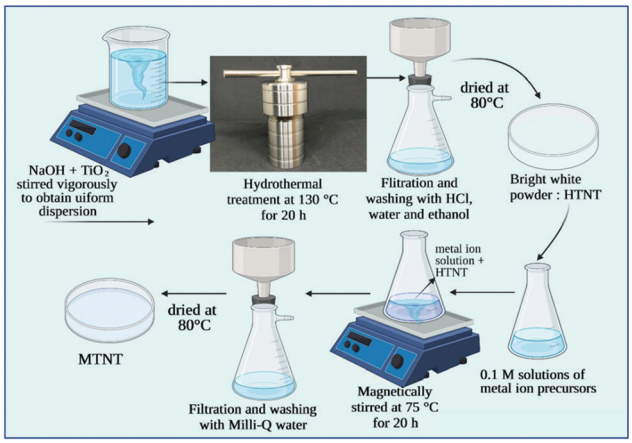

Fig. 1 Schematic of the synthesis of MTNTs.

Brunauer–Emmett–Teller (BET)-based Quantachrome Autosorb iQ specific surface area analyser. The fluoride content in the aqueous samples was quantified using a Thermo Scientific Orion A214 pH/ISE meter with a fluoride ion selective electrode.

2.4 Adsorption studies

The stock solution of fluoride was prepared by dissolving a calculated amount of sodium fluoride (NaF) in double distilled water. In order to prepare 1000 mg L^{-1} of fluoride, 2.21 g of NaF was dissolved in 1000 mL of double distilled water. The working solution was prepared by serial dilution of the stock solution. A fixed dosage of each of the adsorbents was added to water with a specific fluoride content. The contact between the adsorbent and fluoride containing water was maintained for a specified time after which the adsorbent was retrieved *via* filtration. The fluoride content before and after the adsorption process was measured using a fluoride ion meter. All adsorption experiments were carried out in triplicate. Total ionic strength adjustment buffer-II (TISAB-II) was added to the samples in a 1 : 1 (v/v) ratio before the fluoride measurement. The fluoride adsorption capacity (q_e) given by eqn (1) is defined by the amount of fluoride in mg adsorbed per gram of the adsorbent.

$$q_e = \frac{(C_o - C_e)}{C_o} \times \frac{v}{m} \quad (1)$$

where C_o and C_e are the initial and equilibrium fluoride concentrations in mg L^{-1}, v is the volume of liquid in L and m is the mass of the adsorbent in g. The percentage adsorption of fluoride is given by eqn (2).

$$\text{Percentage adsorption} = \frac{(C_o - C_e)}{C_o} \times 100\% \quad (2)$$

3. Results and discussion

3.1 Characterization

3.1.1 Phase and structure identification. The phases and structure of the as synthesized metal ion-functionalized TNTs were studied using their X-ray diffractograms. The X-ray diffraction spectra of the pristine powder HTNTs and MTNTs, where M = Ce, Ca, Cu, Mg, Ni and Ag, are shown in Fig. 2a. The HTNT spectrum showed four prominent peaks positioned at 2θ values of 10.19°, 24.41°, 28.67° and 48.41°. These peaks correspond to the (*hkl*) planes (200), (110), (310) and (020), respectively, which are characteristic of the monoclinic $H_2Ti_3O_7$ phase and belong to the space group $C2/m$. The (200) peak of the HTNTs represents the periodic layered crystallographic structure of the titanate nanotubes. The data are consistent with the ICSD file 98-023-7518 and the previously reported literature.[20–23] To comprehend the structure better, the XRD data were employed to generate the crystallographic structure of the HTNTs with the help of the software VESTA (visualization for electronic and structural analysis) as shown in Fig. 2b. $H_2Ti_3O_7$ had a layered structure, with the layers composed of edge shared TiO_6 octahedra connected in a zigzag pattern. The hydrogen atoms connect these layers and thus lie in the interlayers of the $H_2Ti_3O_7$ structure.

The XRD spectra of the MTNTs, where M = Ce, Ca, Cu, Mg and Ni, have similar XRD patterns as that of HTNT, with the exception of AgTNT, which had a different pattern. There are no extra peaks present in the spectra of MTNTs, corresponding to the metal ions introduced in the HTNTs. Therefore, it could be concluded that the incorporation of metal ions did not disturb the crystallographic structure and retained the monoclinic structure of $H_2Ti_3O_7$. However, it was observed that post wet chemical functionalization of the HTNTs with metal ions, the (200) peak with reduced intensity shifted towards lower

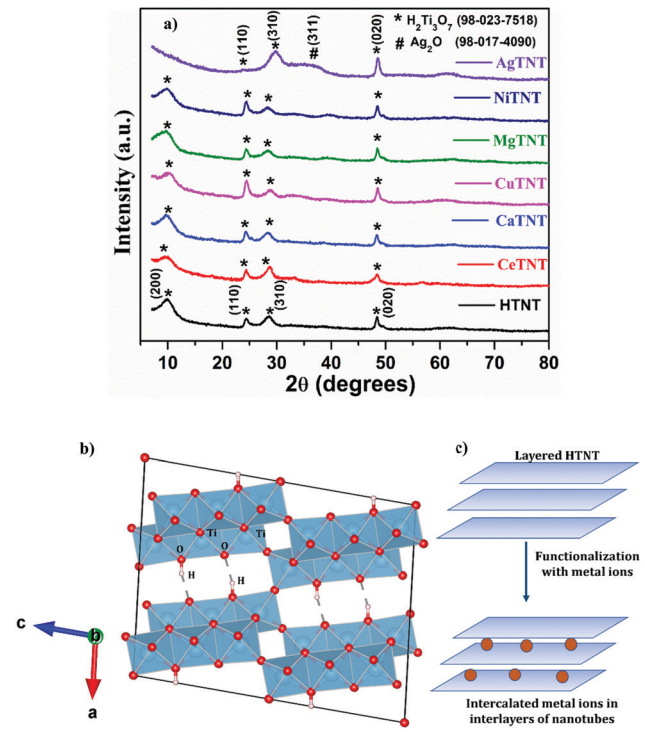

Fig. 2 (a) XRD of pristine HTNT and MTNT; (b) crystallographic structure of $H_2Ti_3O_7$ created using VESTA software; (c) schematic representing the intercalation of metal ions in the interlayer spaces.

2θ values. This could be attributed to the intercalation of the metal ions of the MTNTs into the interlayer spaces of the parent material HTNTs.

As shown in the pictorial representation in Fig. 2c, the layered structure of $H_2Ti_3O_7$ allowed the modification of the material by the incorporation of metal species into the interlayer spaces. The d_{200} value for HTNTs was calculated to be 0.867 nm, whereas the d_{200} values for MTNTs were 0.889, 0.886, 0.872, 0.894 and 0.887, respectively, for CeTNT, CaTNT, CuTNT, MgTNT and NiTNT. As observed from the values, the incorporation of the metal ions resulted in the increased spacing (d_{200}), which resulted in the shift of the (200) peak towards lower 2θ values. In addition, the intensity of the peak corresponding to the (200) plane reduced in MTNTs compared to the parent HTNTs, due to reduction in the crystallinity of the HTNTs caused by the inclusion of metal ions in the interlayer spaces.[24,25]

The XRD pattern of AgTNTs is considerably different from that of HTNTs as shown in Fig. 2a. It has four peaks positioned at 2θ values 24.01°, 29.82°, 32.12° and 48.52°. The peaks positioned at 24.01° and 48.52° correspond to the (110) and (020) planes of the $H_2Ti_3O_7$ phase, whereas the peak positioned at 32.12° corresponds to the (111) plane of Ag_2O (ICSD# 98-017-4090) with a cubic structure.[26,27] Therefore, the AgTNTs were composed of both the phases of $H_2Ti_3O_7$ and Ag_2O. The sharp peak at 29.82° corresponds to the (310) plane of the $H_2Ti_3O_7$ structure, which underwent a shift towards higher 2θ values compared to HTNTs. The (200) peak of the parent HTNTs, positioned at 9.97°, representing the interlayer spacing, disappeared in the AgTNTs due to the introduction of Ag(I) ions in the interlayer spaces. The Ag ions being larger in size compared to the other metal ions, resulted in more disruption in the crystallinity when intercalated in the interlayers of the $H_2Ti_3O_7$ structure. Due to the same reason, the (110) peak also has a substantial reduction in its intensity.[25]

The structure of the functionalized titanate nanostructures, MTNTs and the parent material HTNTs were further investigated using the Raman spectra obtained for these samples as shown in Fig. 3. The Raman spectra of the HTNTs consist of the following vibrational bands: E_g (190 cm^{-1}), A_g (274 cm^{-1}), B_{1g} (450 cm^{-1}) and A_g (650 cm^{-1}). The E_g peak corresponds to the Na···Ti–O bending vibrations, which results from the initial $Na_2Ti_3O_7$ phase formed prior to the acid washing step in the synthesis procedure. The A_g (274 cm^{-1}), B_{1g} (450 cm^{-1}) and A_{1g} (650 cm^{-1}) peaks correspond to the Ti–O–Ti stretching in edge shared TiO_6 octahedra. The presence of broad vibrational bands could be ascribed to the nanotubular structure of the HTNTs. The low intensity mode around 830 cm^{-1} corresponds to the symmetric stretching of the H–Ti–O vibrations of the slightly distorted TiO_6 octahedra of the monoclinic $H_2Ti_3O_7$ phase. The results are in agreement with the previously reported literature.[28,29]

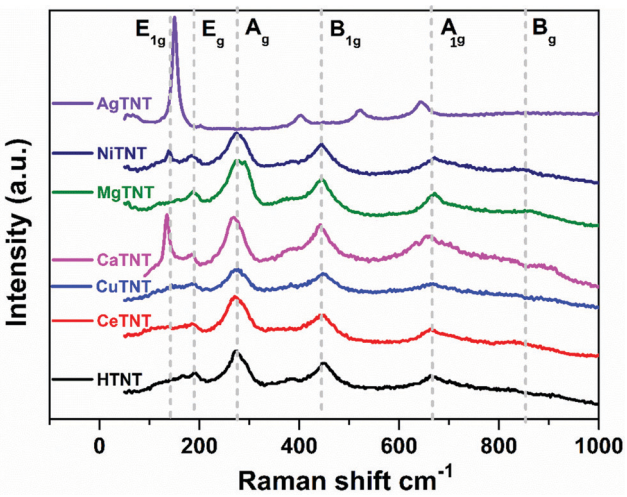

Fig. 3 Raman spectra of MTNTs and HTNTs.

Post functionalization with metal ions in the HTNT structure, the B_{1g} vibrational bands corresponding to the stretching vibration of the Ti–O–Ti bond underwent a slight shift towards the lower wave number region confirming the structural disorder introduced by the insertion of the metal ions – Ca, Mg, and Ni. In the case of MgTNTs, this A_g band splits into two peaks positioned at 275 and 293 cm^{-1}. This could be attributed to the perturbation in the Ti–O bond caused by the incorporation of Mg ions and the formation of a Ti–O–Mg bond, which resulted in the hardening of the vibrational modes.[30] It is interesting to note that the Raman spectra of CeTNT and CuTNT are almost the same as that of the HTNTs indicating that their structure is not much distorted by the intercalation of the Ce and Cu ions, respectively. In the case of NiTNTs and CaTNTs, a new sharp E_{1g} band appears at 138 and 147 cm^{-1}, respectively. This could be attributed to the Ti–O···M vibrations, where M = Ca and Ni.[5] The A_{1g} mode undergoes an upshift in its position in the case of MgTNTs and NiTNTs and a downshift in the case of CaTNTs. This indicates, respectively, the strengthening and weakening of the modes due to metal ions in the lattice structure.[30]

The Raman spectrum of the AgTNTs exhibited significant changes in its vibrational modes compared to that of the HTNTs. Post functionalization with Ag(I), a sharp band appeared at 156 cm^{-1}, and the B_{1g} and the A_{1g} peaks shifted largely towards the lower wavenumber side, whereas the A_g and the E_g peaks disappeared completely. These could be attributed to the formation of a new phase Ag_2O in the Ag-functionalized titanate nanotubes.[30] These results are in agreement with the data obtained from the XRD analysis discussed in Section 3.1.1.

3.1.2 Estimation of the metal loading in the MTNTs. Energy dispersive X-ray spectroscopy (EDS) was carried out to confirm the elemental composition in case of each of the MTNTs and HTNTs. The EDS mappings of the individual metal ions and the overlays of all the metal ions together on the surface of the samples are shown in Fig. 4. As seen from the figures, this analysis confirmed the incorporation of metal ions into the MTNTs during the treatment of HTNTs with the respective metal ion precursors. In addition, the elemental mappings also showed the uniform distribution of each of the elements on the sample surface. The EDS spectra of the MTNTs and HTNTs are given in Fig. S1 (ESI†). As seen from the spectra, there were no extra peaks present in the cases of any of the MTNTs and HTNT, which confirms the purity of the as synthesized samples.

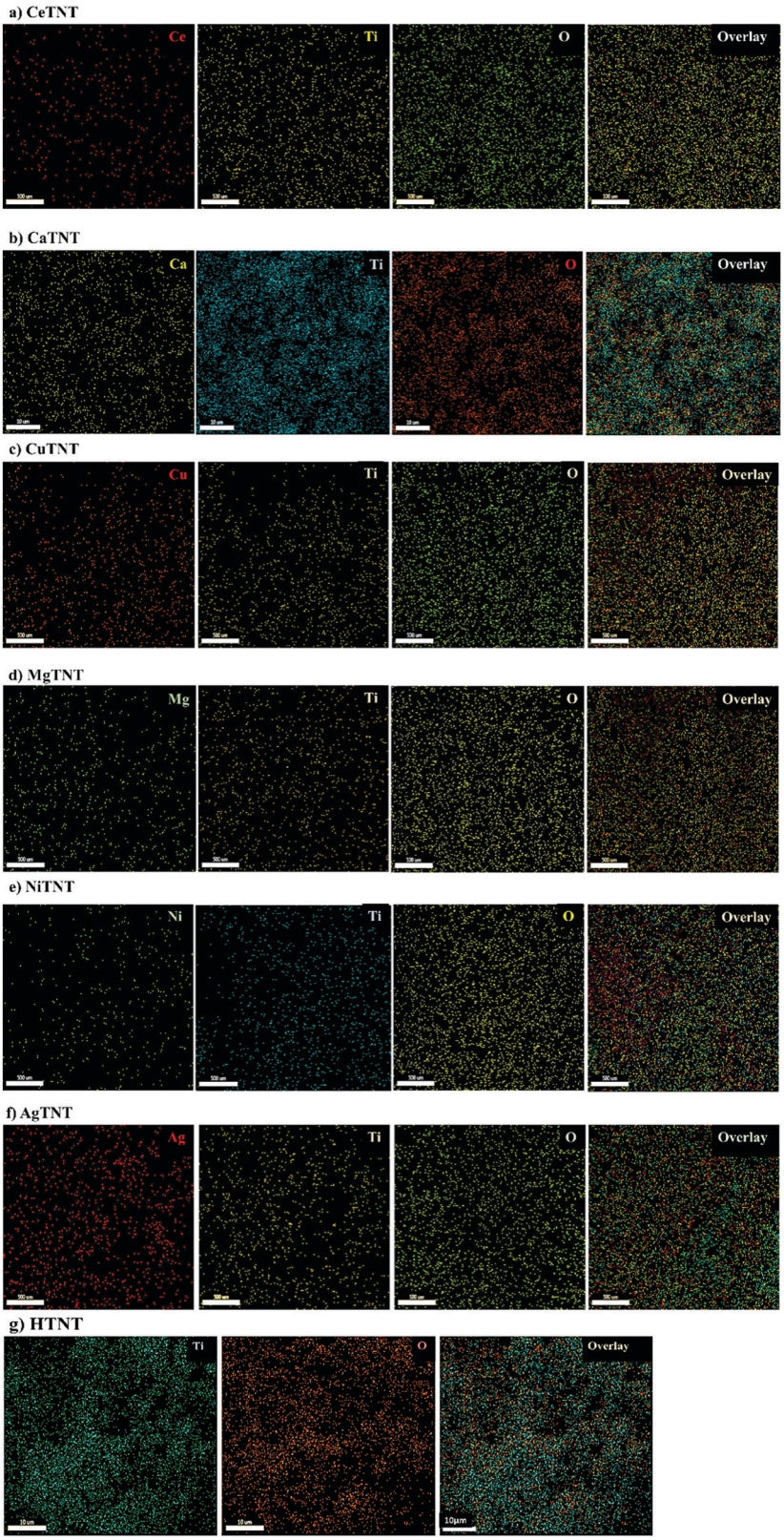

Fig. 4 (a–g) EDS elemental mappings of MTNTs and HTNTs.

The weight and atomic percentage compositions of the samples as calculated from this study are tabulated in Table 1.

It was observed that there was a significant change in the weight of the parent material TNTs after the treatment with the

Table 1 Elemental composition of MTNTs and HTNT as obtained from the EDS analysis

Samples	Element	Atomic (%)	Weight (%)
CeTNTs	Ce	7.66	32.02
	Ti	26.50	37.85
	O	65.83	30.14
CaTNTs	Ca	2.77	4.80
	Ti	19.79	41.10
	O	77.44	54.11
CuTNTs	Cu	3.91	10.83
	Ti	19.54	40.75
	O	76.54	48.42
MgTNTs	Mg	3.27	4.2
	Ti	13.23	33.53
	O	83.50	62.27
NiTNTs	Ni	1.44	4.09
	Ti	17.30	40.02
	O	81.26	55.89
AgTNTs	Ag	7.44	26.93
	Ti	24.55	39.46
	O	68.01	33.60
HTNTs	Ti	40.66	18.62
	O	59.34	81.38

metal ion precursor solutions. This was employed to evaluate the weight percentage of functionalized metal ions in the sample matrix. The corresponding percentage weight changes of the MTNTs were calculated to be 30.98%, 4.21%, 11.02%, 4.40%, 4.56% and 27.50%, respectively, for CeTNTs, CaTNTs, CuTNTs, MgTNTs, NiTNTs and AgTNTs. This difference in weight of the materials post metal ion functionalization was attributed to the incorporation of the respective metal ions into the MTNTs. These values are in agreement with the weight percentages of the metals in MTNTs as calculated from the EDS analysis, given in Table 1.

3.1.3 Morphology and particle size. The morphology and size of the particles in the MTNT samples were studied using the TEM images. The TEM images of each of the MTNTs and the pristine parent material HTNTs are shown in Fig. 5a–g. The corresponding SAED patterns obtained in each case are shown as insets. As seen from these images, the morphology of all the samples is similar with the exception of the AgTNTs. The particles are nanotubular in shape and randomly aligned. Thus, it was observed that the functionalization of the titanate nanotubes with the metal ions, Ce(III), Ca(II), Cu(II), Mg(II) and Ni(II), retained the morphology of the parent materials. The dimensions are tabulated in Table 2.

The incorporation of the metals into the interlayer spacing of the $H_2Ti_3O_7$ phase did not disturb the nanotubular shape of the samples. As calculated from the high-resolution transmission electron microscopic analysis, the inner diameter of the tubes lay in the range of 2.9–3.4 nm. As seen from the SAED patterns of the samples, the diffraction rings corresponded to the crystallographic planes of the titanate phase.

In the case of AgTNTs, the nanotubes were further decorated with nanoparticles that were spherical in shape. These nanoparticles correspond to the Ag_2O phase of the composite material. The phase confirmation was done using the SAED pattern obtained for the sample with the diffraction rings corresponding to both the phases – titanate and Ag_2O. The size of the Ag_2O nanoparticles was in the range of 3.5 nm to 9.5 nm with an average particle size of 8.9 nm. Furthermore the lattice fringes in the nanoparticles as observed in the HRTEM image of the AgTNTs had the d spacing of 0.33 nm, which corresponds to the (110) plane of the Ag_2O phase. These results are in agreement with the data obtained from the XRD analysis, discussed in Section 3.1.1, where AgTNTs were confirmed to be a composite of Ag_2O and $H_2Ti_3O_7$ phases.

The data from Table 2 show that the samples are hollow with tube diameters in the range of 8–9.5 nm, which are much larger than the size of fluoride ions, thus making the area accessible for adsorption of the fluoride ions. It was therefore essential to retain the hollow tubular morphology post functionalization. This is essential for applications like adsorption where the efficiency would be determined by the surface properties of the samples including the morphology and surface area. Therefore, in the following section, the surface areas of the MTNTs are reported.

3.1.4 Specific surface area analysis. The specific surface areas of the pristine HTNTs and MTNTs were studied using the Brunauer–Emmett–Teller (BET) method of nitrogen adsorption and desorption at liquid nitrogen temperatures. The isotherms of adsorption and desorption of HTNT and MTNTs and their BJH pore size distribution are shown in Fig. 6. The calculated specific surface areas, the pore size and the total pore volume are tabulated in Table 3. It was observed that the MTNTs have a high specific surface area lying in the range of 165–247 $m^2\ g^{-1}$, whereas the HTNTs had a specific surface area of 232 $m^2\ g^{-1}$. It can be seen from Fig. 6a–g that the adsorption and desorption isotherms did not retrace each other, resulting in a hysteresis loop. The presence of these hysteresis loops in the HTNTs and MTNTs shows that these samples are mesoporous in nature. This is further validated by the calculation of the pore size by the BJH method. The pore radii of the MTNTs and HTNTs lie between 7 and 9.2 nm. The pore size distribution curves are shown as inset graphs in Fig. 6.

The high surface areas and porous nature of the MTNTs are characteristic of good adsorbents. These could be attributed to the nanotubular morphology, and layered structure of the HTNTs and MTNTs. As observed from Table 3, the metal ion incorporation into the MTNTs and composite formation in the case of AgTNTs retained the high surface area and the porous nature of the parent sample HTNTs.

3.1.5 Optical properties – energy band gap. The optical properties of the materials are affected by doping and functionalization.[16] The UV-visible absorption spectra of the HTNTs and the MTNTs were studied in order to understand their optical properties. The absorption data obtained for the materials were utilized to generate the Tauc plots and calculate their optical energy band gap (E_g) values (Fig. 7a and b). The Tauc relationship, given in eqn (3), relates the energy band gap of the material with the absorbance.[29]

$$\alpha h\nu = A(h\nu - E_g)^{\gamma} \quad (3)$$

where α is the absorption coefficient, h is Planck's constant, ν is the photon frequency, E_g is the band gap and A is the proportionality constant. Here, γ takes the value $\frac{1}{2}$ for direct band gap materials and 2 for indirect band gap materials. As seen from

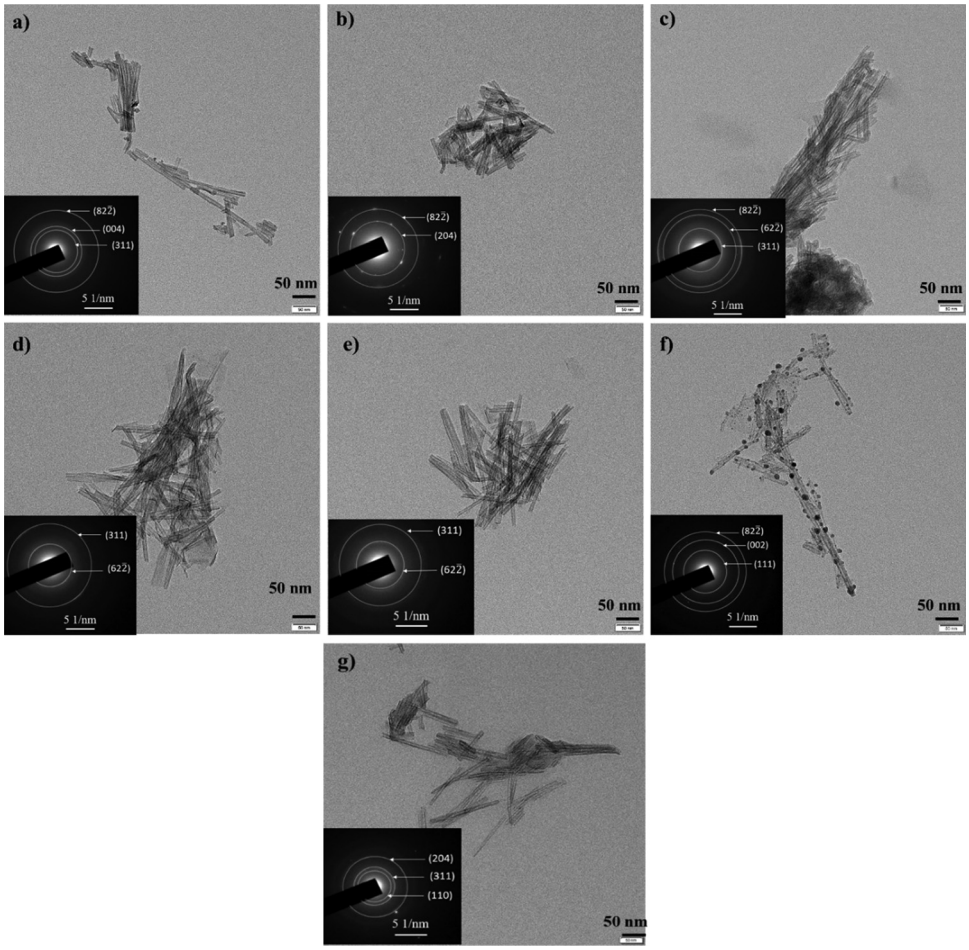

Fig. 5 TEM images and SAED patterns of (a) CeTNTs, (b) CaTNTs, (c) CuTNTs, (d) MgTNTs, (e) NiTNTs, (f) AgTNTs and (g) HTNTs.

Table 2 Particle size of the samples as obtained from TEM images

Sample	Average tube length (nm)	Average tube diameter (nm)	Average particle size (nm)
CeTNTs	96.54	8.33	—
CaTNTs	93.54	7.95	—
CuTNTs	110.86	8.27	—
MgTNTs	115.01	8.19	—
NiTNTs	125.08	8.56	—
AgTNTs	96.37	8.32	8.95
HTNTs	110.25	9.50	—

Fig. 7a, all the samples showed broad absorption peaks followed by a sharp transition in the range of 250–330 nm, which corresponds to the indirect allowed transition of the titanate structure. The presence of broad adsorption peaks could be attributed to the nanosized HTNTs and MTNTs. Furthermore, it was observed that the absorbance peaks broadened towards the visible region post intercalation with metal ions.[31] The indirect band gaps for the samples were calculated using the improvised baseline approach to the existing Tauc method.[32] This involves estimation of the crossover point of the linear fit of the fundamental peak and linear fit applied to the slope below the region of fundamental absorption, which is used as the abscissa or the baseline. The plots, $(\alpha h\nu)^{1/2}$ *vs.* $h\nu$, for indirect band gap calculations, are shown in Fig. 7b. The individual plot for each of the MTNTs is shown in Fig. S1 in the ESI.† The indirect band gaps of the samples are tabulated in Table 4. The calculated indirect band gap E_g is found to be 3.32 eV for the parent material HTNTs. This value is similar to the reported literature value for HTNTs.[5] It was observed that CeTNTs, CaTNTs, CuTNTs, MgTNTs, NiTNTs and AgTNTs had lower energy band gap values than the parent material. Thus, the incorporation of the metal ions Ce, Ca, Cu, Mg, Ag and Ni into the HTNT structure resulted in the lowering of the HOMO–LUMO gaps and hence the red shift in the band gaps. These samples with lower band gaps are attractive materials for applications involving photo-induced reactions. The incorporation of the metal ion resulted in the creation of localized energy levels in the band gaps of HTNTs, which created possibilities of alternative transition pathways. These observations confirm the metal ion functionalization in the interlayer spaces of the layered titanate structure.[24,25]

Furthermore, optical absorption spectroscopy could be used to understand the defects in the system, which could be estimated in terms of the parameter, Urbach energy, E_u. The metal ion

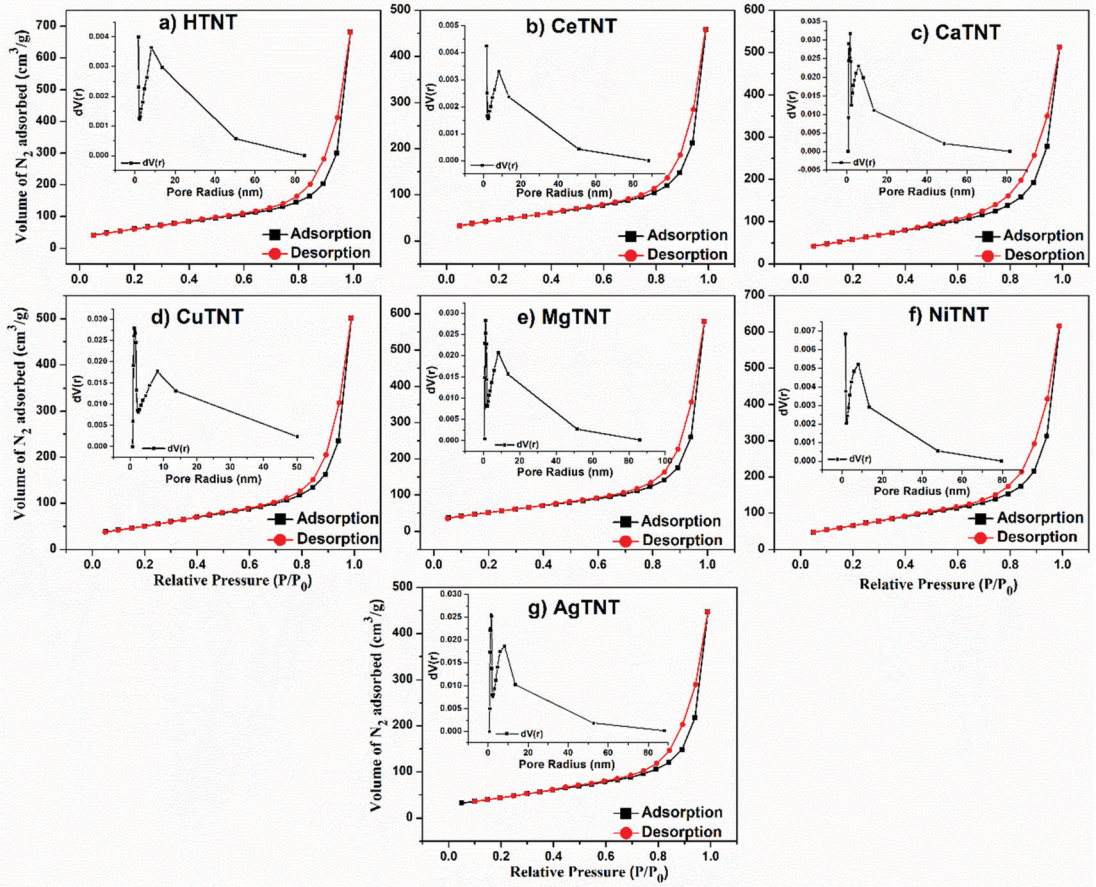

Fig. 6 (a–g) BET-based N_2 adsorption–desorption isotherms and BJH pore size distribution of HTNTs and MTNTs.

Table 3 Surface area, average pore size and pore volumes of MTNTs and HTNTs

Samples	Specific surface area ($m^2\ g^{-1}$)	Average pore radius (nm)	Total pore volume (cc g^{-1})
AgTNTs	165	8.43	0.69
CeTNTs	177	8.48	0.71
CuTNTs	189	8.26	0.78
MgTNTs	195	9.23	0.90
CaTNTs	217	7.32	0.79
NiTNTs	247	7.18	0.95
HTNTs	232	9.12	1.06

intercalation of HTNTs might have introduced localized defect states in the parent titanate structure. These defect states in the MTNTs lead to band tailing into the forbidden energy band gap regions and contribute towards lowering of the band gaps. These band tails are called Urbach tails and are characterized in terms of Urbach energy, which gives an estimate of the overall defects in the system.[33–35] In order to understand this better, the Urbach energy was calculated for each of the MTNTs and HTNTs. Eqn (4) can be used to calculate the Urbach energy:

$$\alpha = \alpha_0 \exp\left(\frac{h\nu}{E_u}\right) \quad (4)$$

where α_0 is a constant. The linear form of the above equation is given in eqn (5)

$$\ln(\alpha) = \ln(\alpha_0) + \frac{h\nu}{E_u} \quad (5)$$

Therefore, the inverse slope of the linear fit obtained from the plot of $\ln(\alpha)$ *vs.* $h\nu$ gives the Urbach energy. The values of Urbach energy for MTNTs and HTNT are tabulated along with the band gaps in Table 4.

It can be observed that the values of the Urbach energy, E_u, increased in the MTNTs compared to the value of HTNTs. This could be attributed to the increased number of defect sites and oxygen vacancies in the MTNTs caused by the metal ion incorporation into the HTNT structure. The presence of defects in the samples is beneficial for the adsorption process as these sites act as additional adsorption sites, which further enhance the fluoride adsorption capacity of the samples.[2] These defect sites result in the formation of activated hydroxyl groups that can act as active sites for fluoride adsorption.

3.1.6 Structure analysis – functional groups. The structural properties of the MTNTs in terms of the presence of different functional groups in the samples were further studied using FTIR spectroscopy. The FTIR spectra of pristine HTNTs and MTNTs are shown in Fig. 8. As seen in the figure, all the samples have a broad peak around 3200–3400 cm^{-1} which

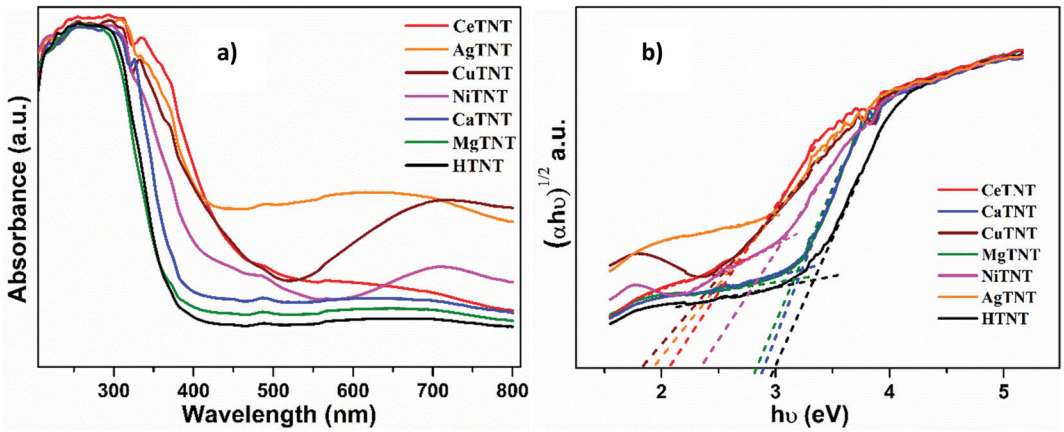

Fig. 7 The UV-VIS (a) absorption spectra and (b) Tauc plots for MTNTs and HTNTs.

Table 4 Energy band gaps and Urbach energy values calculated for HTNTs and MTNTs

Samples	Indirect E_g (eV)	Urbach energy E_u (eV)
CuTNTs	2.57	0.960
CeTNTs	2.82	0.695
AgTNTs	2.93	0.838
NiTNTs	2.99	0.760
CaTNTs	3.17	0.536
MgTNTs	3.21	0.542
HTNTs	3.22	0.522

arises from the antisymmetric stretching vibrations of the OH groups on the sample surface.[36,37] The sharp peaks around 1640 cm^{-1} correspond to the bending vibrations of the H–OH and surface –OH groups present in the samples. This confirmed the presence of surface hydroxyl groups in the metal ion-intercalated samples.[2,38]

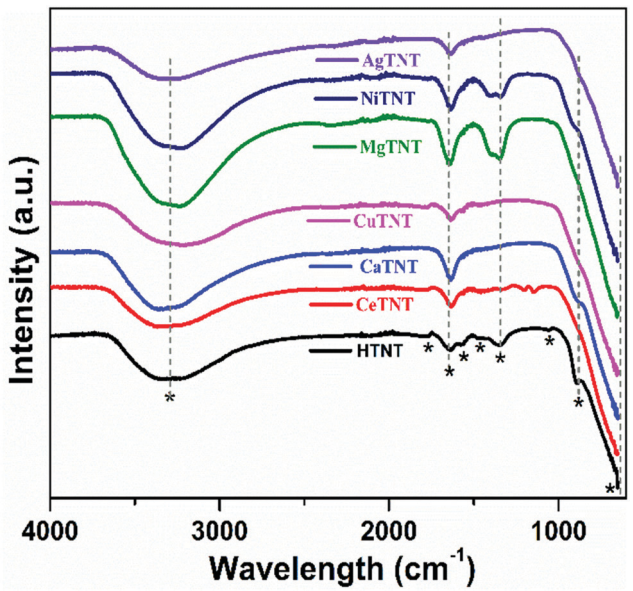

Fig. 8 The FTIR spectra of pure HTNTs and MTNTs.

The peaks at 1570 cm^{-1}, 1472 cm^{-1}, and 1046 cm^{-1} correspond to the characteristic vibrations of Ti–OH, Ti–O and Ti–O–Ti bonds, respectively, of the titanate structure, some of which disappeared in the MTNTs due to the metal ion incorporation.[2,30] The peak at 888 cm^{-1} corresponds to the stretching vibration of the Ti–O bond from the TiO_6 octahedra. This peak is affected by the intercalation of the metal ions as seen by its reduced intensity in the CaTNTs and NiTNTs and its absence in the CeTNTs, CuTNTs, MgTNTs and AgTNTs.[10,39] The peak around 651 cm^{-1} corresponds to the M–O bond (M = Ti, Ce, Ca, Cu, Mg, Ni and Ag). The Ti–OH peak at 1342 cm^{-1} in the HTNTs reduced in intensity or disappeared in the CeTNTs, CaTNTs, CuTNTs and AgTNTs, whereas this peak intensity increased slightly in the MgTNTs and NiTNTs. In the spectra of the CeTNTs, two additional peaks appeared at 1200 cm^{-1} and 1143 cm^{-1} corresponding to the Ce–O and Ce–OH vibrations.[40] The Mg–O and Mg–OH vibrations resulted in a peak at 1388 cm^{-1} in the spectrum of the MgTNTs.[41] The 1329 cm^{-1} peak of the Ni-TNTs resulted from the Ni–OH vibrations. This confirmed the presence of M–O and M–OH bonds (M = metal ions), which represent the metal ion functionalization. Furthermore, the large availability of M–OH bonds is beneficial for the adsorption process as the hydroxyl ions act as fluoride adsorption sites. Therefore, the incorporation of metal ions into the TNTs resulted in the abundant availability of adsorption sites in the MTNTs.

3.2 Adsorption studies

An ideal adsorbent must exhibit the following properties: high adsorption capacity with quick adsorption and utilization of minimum adsorbent quantity. Therefore, it is imperative to systematically evaluate the impact of solution pH, time, adsorbent dosage and initial fluoride concentration on the adsorption capacity of the adsorbents. This was studied by using a batch adsorption process, and the inferences obtained from the results were utilized to obtain the best operating parameters and understand the adsorption mechanism. The batch adsorption experiments were carried out independently with each metal ion-incorporated TNT adsorbent in order to optimise the best operating parameters in each case.

3.2.1 Effect of solution pH. The adsorption process is highly dependent on the pH of the solution. Hence, it is necessary to investigate the impact of pH on the adsorption capacity. The pH of water, with fixed fluoride content, was varied from 2 to 7; a fixed dosage of MTNTs was added to it and agitated for a specified time period. The variations of fluoride adsorption efficiency of the MTNTs and HTNTs with the pH of water are shown in Fig. 9. As seen from the figure, with the increase in the pH, the fluoride adsorption capacity decreased for the HTNTs and MTNTs (M = Ca, Cu, Mg, Ni and Ag) with maximum adsorption at pH 2. However, the CeTNTs had maximum fluoride adsorption at pH 3 after which the fluoride adsorption capacity decreased.

The trend in the variation of adsorption capacity with solution pH could be explained based on the surface charge of the parent material as obtained from the zeta potential measurements. As reported in our previous work,[2] the zero point charge, that is pH_{ZPC} of HTNTs is 2.11. The surface of the material is therefore positively charged at pH $<$ pH_{ZPC} = 2.11 and negatively charged at pH $>$ pH_{ZPC} = 2.11. Therefore, the positively charged surface attracts the negatively charged fluoride ions and results in high fluoride adsorption at acidic pH, whereas the negatively charged surface results in repulsion between the surface of the material and the fluoride ions resulting in a decrease in the adsorption capacity with increasing pH.

As seen from the figure, CeTNTs had the highest adsorption capacity compared to HTNTs and other MTNTs, which could be attributed to the higher ionic charge and higher affinity of Ce towards the fluoride ions compared to the other ions considered in this study. At pH 3 the adsorption capacity follows the order – CeTNTs $>$ CaTNTs $>$ CuTNTs $>$ NiTNTs $>$ AgTNTs $>$ MgTNTs $\sim$ HTNTs. The materials had fluoride adsorption capacity in the range of 5.8–8.6 mg g^{-1} with 10 mg L^{-1} of initial fluoride concentration, thus showing good adsorption efficiencies of the HTNTs and MTNTs. As the majority of the samples had maximum adsorption at pH 2, all the further adsorption experiments were done at pH 2.

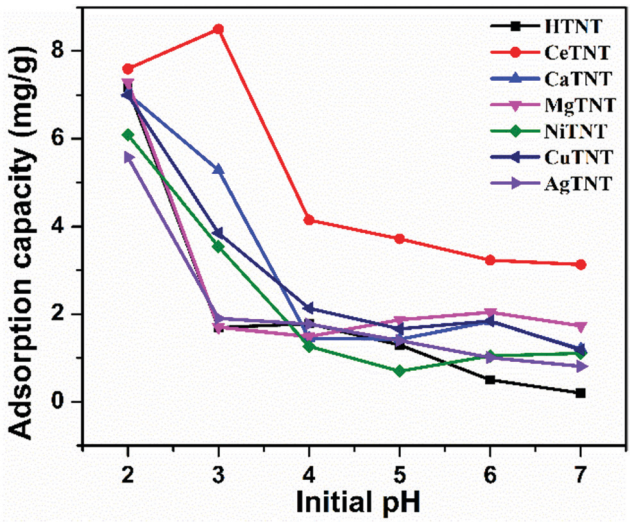

Fig. 9 Variations of adsorption capacities with the pH of the solution (initial concentration 10 mg L^{-1}, time 2 h, and dosage 1 g L^{-1}).

3.2.2 Effect of contact time. The time for which the adsorbents are in contact with the fluoride containing water is referred to as the contact time. It is essential that an adsorbent removes contaminants from water as fast as possible. To evaluate this effect of contact time in adsorption of fluoride ions, 1 g L^{-1} of each of the adsorbents, HTNTs and MTNTs, was individually added to water with 10 mg L^{-1} of fluoride content at pH 2, whereas the contact time was varied from 1 min to 180 min. The results are shown in Fig. 10a and b.

As seen from the figure, both HTNTs and the metal ion incorporated MTNTs exhibited rapid adsorption kinetics, that is, high adsorption efficiency was achieved in a very short span of time. The samples, CeTNTs, CaTNTs, CuTNTs, MgTNTs, NiTNTs, and AgTNTs including the parent sample HTNTs showed about 90% of their respective equilibrium adsorption capacities in just 1 min. Furthermore, the MTNTs reached the fluoride adsorption equilibrium within 60 min of contact time, whereas for the HTNTs the adsorption equilibrium was reached within 120 min of contact time. The kinetics of the adsorbents reported in this work are much faster than that of the traditional adsorbents.[1] Therefore, the incorporation of the metal ions resulted in faster adsorption compared to the HTNTs. The rapid adsorption could be attributed to the abundant availability of the adsorption sites due to the nanotubular morphology, high surface area and intercalation of metal ions with significant ionic charge. The fast kinetics exhibited by these samples makes them ideal adsorbents for the development of real time filters.

3.2.2.1 Adsorption kinetics. Furthermore, these data were analysed using the two common adsorption kinetics: pseudo first order (PFO) and pseudo second order (PSO) adsorption kinetics. The PFO and PSO can be expressed by the eqn (6) and (7), respectively.[10]

$$q_t = q_e(1 - e^{-k_1 t}) \quad (6)$$

$$q_t = \frac{k_2 q_e^2 t}{1 + k_2 q_e t} \quad (7)$$

where q_e is the equilibrium fluoride adsorption capacity in mg g^{-1}, q_t is the fluoride adsorption capacity at time t in mg L^{-1}, k_1 (min^{-1}) is the PFO equilibrium rate constant and k_2 (g mg^{-1} min^{-1}) is the PSO equilibrium rate constant. The graphs representing the isotherm fits to the data points are shown in Fig. 11a–g. The parameters calculated from the isotherms are tabulated in Table 5.

It can be seen that both the isotherms fit the data well with R^2 value $\sim$1. However, the PSO isotherms fit the data slightly better than the PFO isotherms. The results are in concurrence with previously reported data on fluoride adsorption using titanate nanostructures.[2]

The rate constants calculated from these isotherms indicate the rapid adsorption kinetics of the adsorbents. Additionally, the higher rate constants calculated for MTNTs compared to

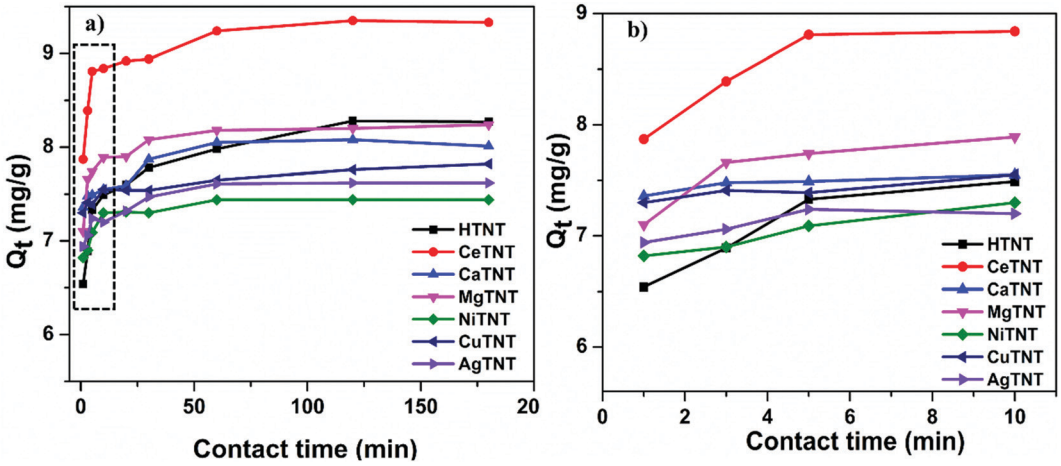

Fig. 10 (a and b) Variations of the adsorption capacities with contact time (initial concentration 10 mg L^{-1}, dosage 1 g L^{-1} and pH 2).

HTNTs indicate the faster adsorption in the case of the former, thus confirming the superior kinetics of MTNTs.

3.2.3 Effect of initial fluoride concentration. The effect of initial fluoride concentration on the fluoride adsorption efficiency was investigated. 1 g L^{-1} of the samples was added to water with known fluoride content at pH 2 for a period of 2 hours. The fluoride content was varied from 2 to 200 mg L^{-1}. The fluoride content in the effluent was measured and the variations in the adsorption efficiencies as a function of initial fluoride concentration are shown in Fig. 12. As seen from the figure, the adsorption efficiencies increased with the increase in fluoride concentration without reaching any saturation value. Therefore, these samples are efficient in both low and high fluoride concentrations. This was due to the abundant availability of the adsorption sites in the MTNTs and the parent material HTNTs.

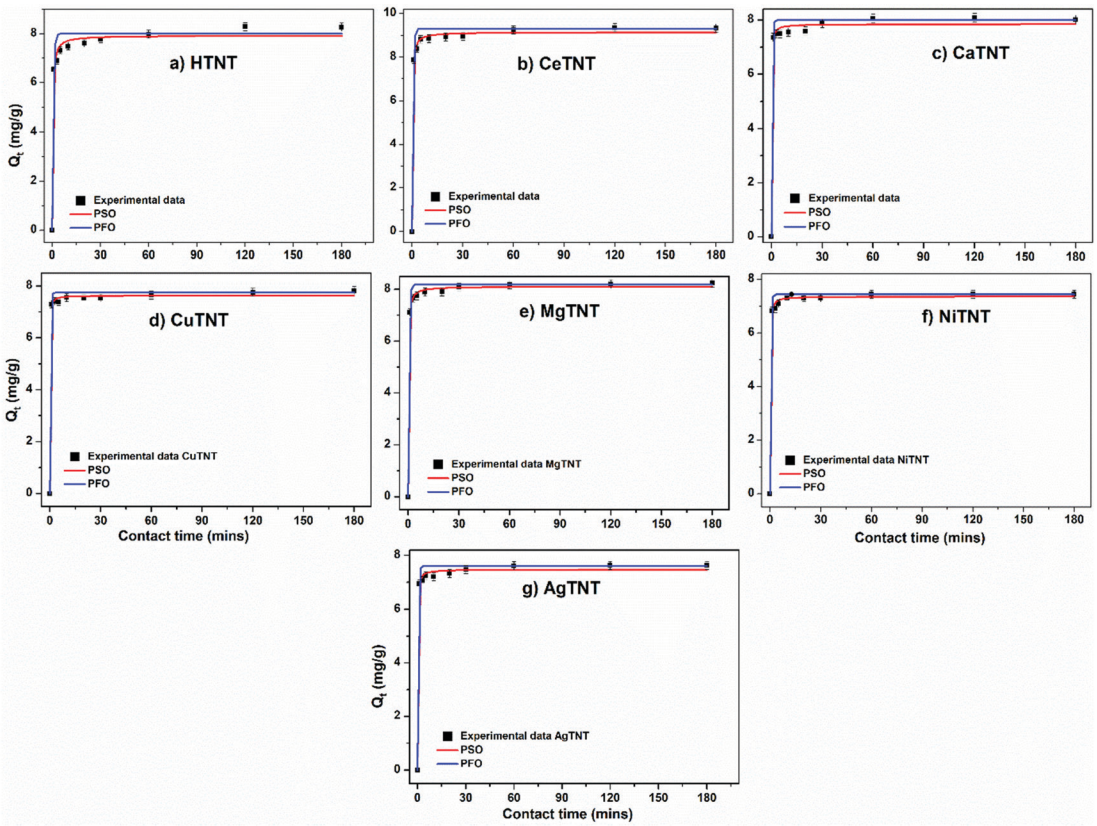

Fig. 11 (a–g) Pseudo first order (PFO) and pseudo second order (PSO) isotherm fits to the experimental data (initial concentration 10 mg L^{-1}, dosage 1 g L^{-1} and pH 2).

Table 5 Parameters calculated from PFO and PSO isotherm fits to the experimental data

		Pseudo-first order parameters			Pseudo-second order parameters		
Samples	$q_{e,exp}$, mg g^{-1}	k_1, min^{-1}	$q_{e,cal}$, mg g^{-1}	R^2	k_2, g mg^{-1} min^{-1}	$q_{e,cal}$, mg g^{-1}	R^2
CeTNTs	9.36	1.820	9.18	0.979	0.605	9.14	0.996
MgTNTs	8.11	1.999	8.08	0.989	0.805	8.11	0.998
CaTNTs	8.02	2.495	7.92	0.982	1.493	7.84	0.993
CuTNTs	7.69	2.817	7.60	0.992	2.357	7.63	0.998
AgTNTs	7.53	2.410	7.43	0.986	1.471	7.47	0.996
NiTNTs	7.38	2.466	7.32	0.990	1.407	7.35	0.998
HTNTs	8.26	1.616	8.12	0.987	0.477	7.92	0.987

3.2.3.1 Adsorption isotherms. The experimental data were studied with the help of two popular adsorption isotherms – Langmuir and Freundlich isotherms for better understanding of the adsorption mechanism. According to the Langmuir adsorption isotherm, the adsorbent is assumed to have homogenous adsorbent sites and there is only monolayered adsorption. Furthermore, it assumes that there is no interaction between the adsorbent and the adsorbate.[42] This isotherm can be expressed as shown in eqn (8).

$$q_e = q_{max} b c_e / (1 + b c_e) \quad (8)$$

where q_e (mg g^{-1}) is the equilibrium adsorption capacity, c_e (mg L^{-1}) is the equilibrium fluoride concentration, b (L mg^{-1}) is the Langmuir isotherm constant and q_{max} (mg g^{-1}) is the maximum fluoride adsorption capacity.

The Freundlich adsorption isotherm assumes that the adsorbent surface is heterogenous and multi-layered adsorption with lateral interaction takes place between the adsorbate and the adsorbent.[43] This isotherm can be expressed as shown in eqn (9).

$$q_e = K_f c_e^{1/n} \quad (9)$$

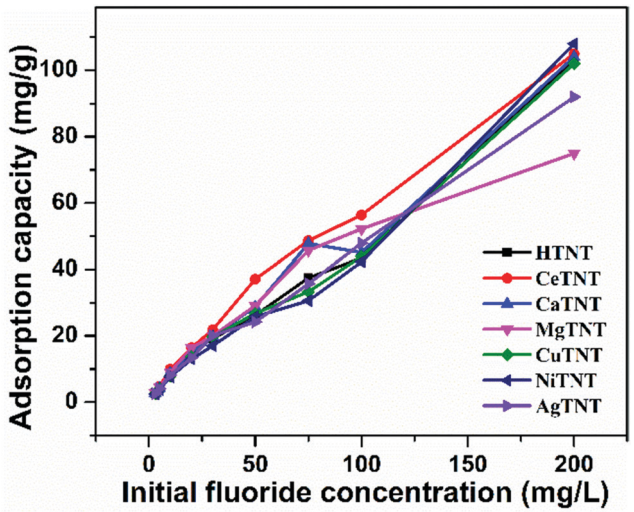

Fig. 12 Variations of adsorption capacity with initial fluoride concentration (time 2 h, dosage 1 g L^{-1} and pH 2).

where K_f((mg g^{-1}) (L mg^{-1})$^{1/n}$) is the Freundlich isotherm constant and $(1/n)$ is a heterogeneity factor indicative of the adsorption intensity.

The graphs representing the Langmuir and Freundlich fits of the experimental data are shown in Fig. 13a–g. The parameters calculated from the isotherms are tabulated in Table 6. It was observed that both the isotherms fit the experimental data well with the R^2 value close to unity; but the Freundlich adsorption isotherms fit the data better with higher R^2 values. The maximum adsorption capacity (Q_{max}) values of the samples were calculated from the Langmuir isotherm fits.

The MTNTs exhibited very high Langmuir adsorption capacities with the Q_{max} values lying between 98.35 and 183.34 mg g^{-1}, whereas the Q_{max} value for the HTNTs was calculated to be 97 mg g^{-1}. The fluoride adsorption capacity of the parent material, HTNTs, was much higher than that of the crystalline titanium oxide, which is reported to have a q_{max} value of 0.270 mg g^{-1}.[44] The incorporation of metal ions into the HTNTs further enhanced the fluoride adsorption capacities compared to that of the HTNTs. The order of fluoride adsorption capacities of the adsorbents was observed to be CaTNTs > AgTNTs > CuTNTs > CeTNTs > NiTNTs > MgTNTs > HTNTs. The comparison is graphically represented in Fig. 14. The cation intercalation in the adsorbents resulted in the increase in the number of adsorption sites available on the adsorbent surface leading to high adsorption efficiency. The highest adsorption capacity of CaTNTs could be attributed to the specific affinity of Ca^{2+} for fluoride ions from water.[45] In the case of AgTNTs, the high Q_{max} value could be attributed to both the intercalated Ag^+ ions and the presence of Ag_2O particles decorated on the surface of the nanotubes.

It was also observed that although some samples had lower efficiencies at low fluoride concentrations, their efficiency was enhanced at higher fluoride concentrations. Therefore, the changes in the trends in adsorption efficiencies are compared to those obtained from pH studies. Since both the isotherms fit the adsorption data, the adsorption mechanism must be a combination of both physisorption and chemisorption.

3.2.3.2 Mechanism of adsorption. The probable adsorption mechanism was therefore deduced based on the results obtained from the FTIR and XRD characterizations of the pristine and fluoride adsorbed powder samples. The XRD spectra of the HTNTs and MTNTs post fluoride adsorption (HTNT-F and MTNT-F) are shown in Fig. 15a. It was observed that post fluoride adsorption HTNT-F and MTNT-F where M = Ce, Ca, Cu, Mg and Ni retained the four characteristic peaks corresponding to the (*hkl*) planes (200), (110), (310) and (020) of the monoclinic titanate structure (ICSD #98-023-7518). However, the peaks underwent slight shifts in their positions, which could be attributed to the successful adsorption of the fluoride ions from water. The crystallinity of AgTNT-F increased, as shown by the presence of sharp peaks of Ag_2O, as seen in Fig. 15a. This could be due to the reordering of the crystal structure which would take place during the fluoride adsorption. The peaks positioned at 2θ values of 27.8, 32.4,

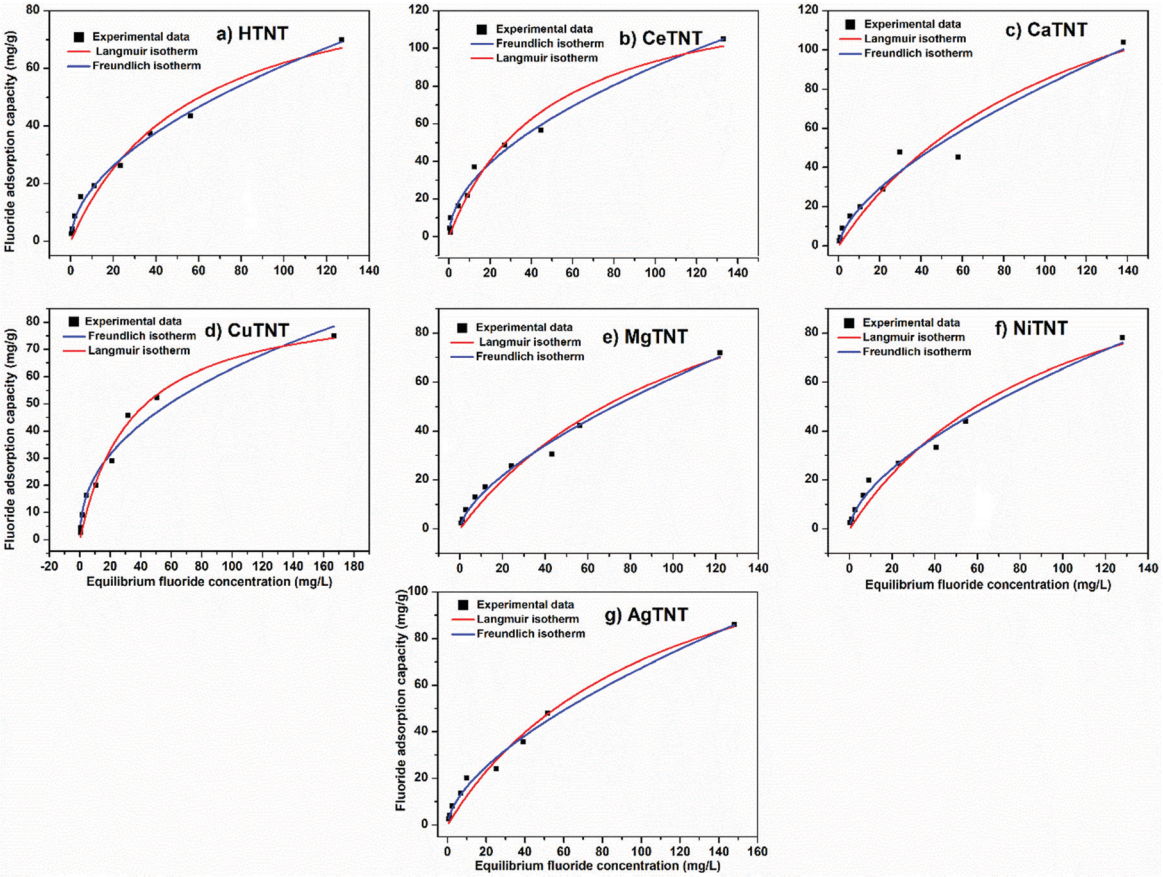

Fig. 13 (a–g) Adsorption isotherm fits of the experimental data of HTNTs, CeTNTs, CaTNTs, CuTNTs, MgTNTs, NiTNTs and AgTNTs, respectively (time 2 h, dosage 1 g L^{-1} and pH 2).

Table 6 Parameters calculated from Langmuir and Freundlich isotherms

	Langmuir isotherm			Freundlich isotherm		
Sample	q_{max}, mg g^{-1}	b, L g^{-1}	R^2	K_f, (mg g^{-1}) (L mg^{-1})$^{(1/n)}$	n	R^2
CaTNTs	183.24	0.009	0.931	4.371	1.572	0.959
AgTNTs	147.69	0.009	0.972	3.958	1.624	0.989
CuTNTs	138.52	0.008	0.963	3.132	1.543	0.988
CeTNTs	137.87	0.021	0.963	8.227	1.920	0.987
NiTNTs	134.62	0.010	0.955	3.991	1.646	0.989
MgTNTs	98.35	0.029	0.974	8.643	2.319	0.968
HTNTs	97.15	0.018	0.955	5.416	1.902	0.994

46.4, 54.7, 57.5, 67.9, 74.7 and 76.7 of the AgTNTs could be attributed to the planes (110), (111), (211), (220), (212), (311), (312) and (400), respectively, of the cubic Ag_2O phase.[26,27] This is in consistence with the ICSD #98-017-4090.

The FTIR spectra of the fluoride adsorbed samples, that is, HTNT-F and MTNT-F are shown in Fig. 15b. The peaks corresponding to the M–OH, M–O and H–OH vibrations, which were present in the pristine samples, either reduced in intensity or disappeared in the MTNT-F and HTNT-F. This reduction in the intensity of these peaks corresponding to the OH bonds in the fluoride adsorbed samples MTNT-F and HTNT-F was probably due to the successful ion exchange between the surface

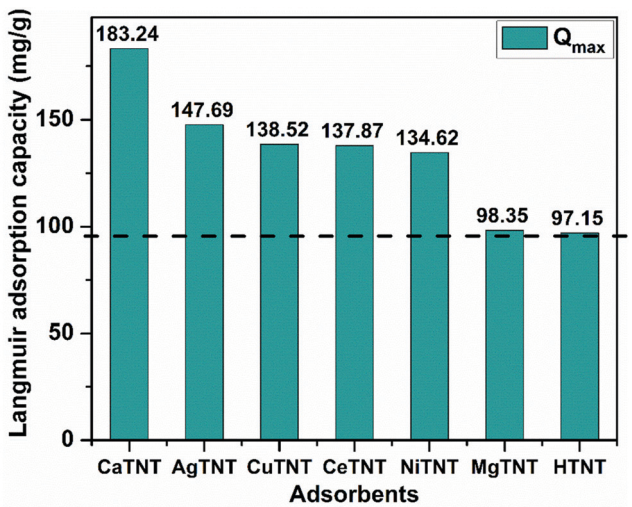

Fig. 14 Graphical representation and comparison of the Langmuir adsorption capacities of the adsorbents.

hydroxyl groups and the fluoride ions in water that would take place during the process of adsorption.[2,10] Therefore, the adsorption would take place *via* an ion exchange mechanism. The FTIR analysis of the pristine samples indicated the

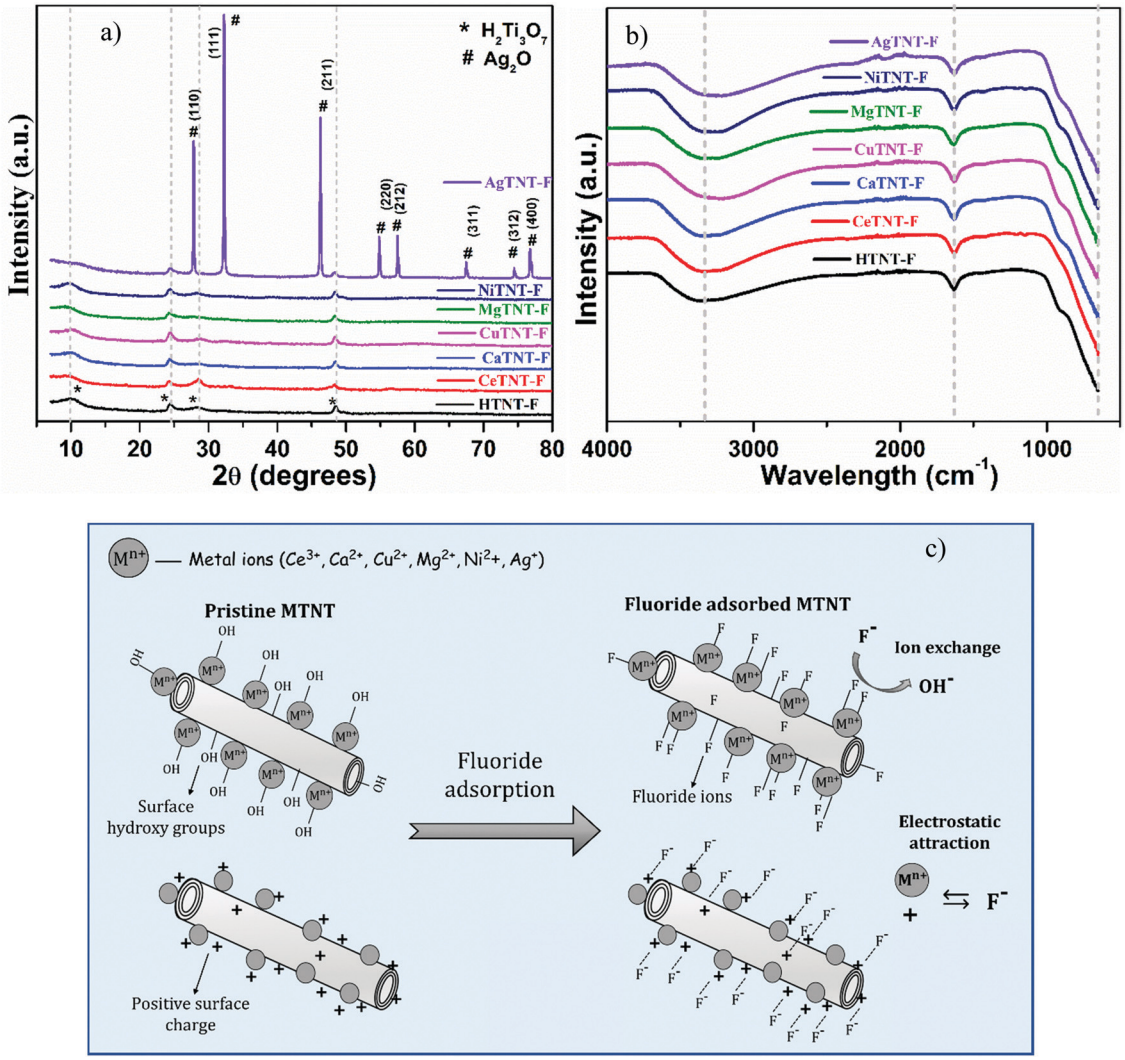

Fig. 15 (a) XRD spectra, (b) FTIR spectra of fluoride adsorbed MTNTs and HTNTs and (c) schematic of the proposed fluoride adsorption mechanism with MTNTs.

abundance of surface hydroxyl groups in the developed materials, which resulted in enhanced fluoride removal by the MTNTs. In addition, as indicated by the Urbach energy values, the metal-functionalized samples had a significant number of defects that also act as potential fluoride adsorption sites. As mentioned previously, the surface charge of the nanotubes is positive in the acidic pH range, and thus, another pathway for adsorption of the fluoride ions could be *via* electrostatic attraction. Therefore, the proposed pathway for fluoride adsorption using HTNTs and MTNTs is a combination of both ion exchange and electrostatic attraction. The schematic of the proposed fluoride adsorption mechanism is shown in Fig. 15c. The enhanced fluoride adsorption in the case of MTNTs was due to the higher surface area of the materials, their nanotubular morphology, and the presence of metal cations in the MTNTs leading to an increased number of active adsorption sites, that is the surface hydroxyl groups and the defects. The synergy of these factors resulted in enhanced fluoride adsorption in the metal ion-functionalized titanate nanotubes.

3.2.4 Effect of adsorbent dosage. For an efficient adsorption process, high efficiency must be achieved using a much lower quantity of the adsorbent. A fixed dosage of adsorbent was added to 10 mg L^{-1} of fluoride ions at pH 2, for two hours and the dosage was varied from 0.5 g L^{-1} to 5 g L^{-1}. The variations of the adsorption efficiencies with dosage of the MTNTs and HTNTs are shown in Fig. 16. As seen from the figure, the adsorption efficiencies increased with the increase in the adsorbent dosage and the adsorption efficiencies finally reached an equilibrium. This is because of the increase in the adsorption sites with the increased dosage. In all the samples, the adsorption efficiency reached the equilibrium at the adsorbent dosage of 4 g L^{-1}. The maximum fluoride adsorption percentages obtained for CeTNTs, CaTNTs, CuTNTs, MgTNTs, NiTNTs, AgTNTs and HTNTs are 98, 94.8, 91.5, 87.5, 90.1, 91.2 and 92, respectively. However, even at a low adsorbent dosage of 1 g L^{-1} the samples had high adsorption capacity. Therefore, this dosage was used for all the adsorption studies. The requirement of less adsorbent quantity makes the adsorbents economically viable.

The batch adsorption studies confirmed the optimised fluoride adsorption conditions for MTNTs to be pH 2, a contact time of 60 min, and a dosage of 1 g L^{-1} applicable for both low

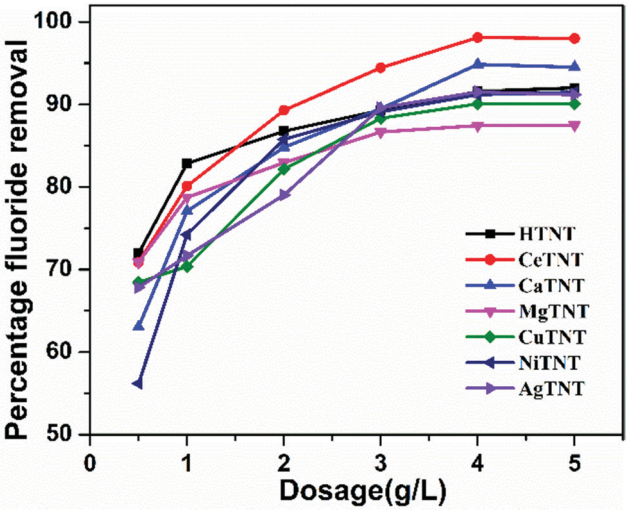

Fig. 16 Variations of percentage fluoride adsorption with the adsorbent dosage (initial concentration 10 mg L^{-1}, time 2 h and pH 2).

and high fluoride concentrations. To sum up the adsorptive properties of the MTNTs, they exhibited excellent adsorption properties in the acidic pH region with rapid kinetics, high adsorption capacities and low dosage, thus making these MTNTs attractive materials for adsorption of fluoride from water. Apart from the fluoride contamination of groundwater, wastewater also contains a very high concentration of fluoride ions and is acidic in nature.[46] Therefore, these materials are potential materials for treating fluoride contaminated water.

4. Conclusions

Metal ion-functionalized titanate nanotubes, MTNTs (where M = Ce^{3+}, Ca^{2+}, Cu^{2+}, Mg^{2+}, Ni^{2+} and Ag^{+}) were successfully developed *via* a hydrothermal process followed by wet chemical treatment. The wet chemical treatment led to metal ion incorporation into the interlayer spaces of the titanate structure resulting in CeTNTs, CaTNTs, CuTNTs, MgTNTs and NiTNTs with only $H_2Ti_3O_7$ phase; whereas wet-chemical treatment with the silver precursor led to nanocomposite formation of the HTNTs with Ag_2O, in addition to Ag intercalation into the interlayer spaces. This was confirmed by the XRD and Raman analysis. The incorporation of metal ions and their corresponding weight percentages in the MTNTs were confirmed by EDS analysis. The TEM images confirmed the morphology of the samples to be nanotubular with the exception of the AgTNTs, whose morphology showed the decoration of the nanotubes with Ag_2O nanoparticles. The BET analysis proved the high surface areas and porous nature of the MTNTs with the surface areas lying in the range of 165–247 $m^2 g^{-1}$. The pore size of the MTNTs was in the range of 7.18–9.23 nm. In addition, the MTNTs showed lower optical band gaps compared to that of the HTNTs making them attractive for photoinduced activities with band gap values between 2.57 and 3.21 eV. Furthermore, the MTNTs had a significant number of defects as indicated by the Urbach energy values. The fluoride adsorption experiments on the MTNTs revealed their promising adsorbent characteristics, such as high adsorption capacity, rapid adsorption kinetics and use of low adsorbent dosage. It is evident from the kinetic study that MTNTs are very quick in removing fluoride from water, unlike the traditional adsorbents. The Langmuir adsorption capacities of all MTNTs are enhanced compared to HTNTs and lie in the range of 98.35–183.34 mg g^{-1}. The enhanced adsorption properties of the MTNTs could be attributed to two factors: (a) increased numbers of adsorption sites and (b) increased positive charge density on the MTNTs due to metal ion incorporation. These two factors contribute to the synergetic effect of electrostatic attractions and ion exchange mechanism, which makes MTNTs a superior adsorbent compared to HTNTs.

Author contributions

Anjana Biswas: conceptualization, data curation, formal analysis, methodology, software, writing – original draft preparation, validation, and writing – review and editing. C. Prathibha (corresponding author): visualization, conceptualization, funding acquisition, project administration, resources, supervision, validation, and writing – review and editing.

Funding

This work was funded by Kurita Water and Environment foundation (KWEF) under the Kurita overseas research grant, grant number – 18PO17.

Conflicts of interest

There are no conflicts of interest to declare.

Acknowledgements

The authors are thankful to the Central Research Instrument Facility, Prashanthi Nilayam for providing the necessary characterization facilities. The authors also thank the Central research laboratory, Anantapur for facilitating the synthesis and characterization facilities.

References

1 C. Prathibha, A. Biswas and M. V. Shankar, Titanate Nanostructures as Potential Adsorbents for Defluoridation of Water, *Nanostructured Materials for Environmental Applications*, Springer International Publishing, 2021, pp. 383–400, DOI: 10.1007/978-3-030-72076-6_15.

2 A. Biswas and C. Prathibha, Fe(III) and Zr(IV) surface functionalized 1-D hydrogen titanate nanotubes for remediating fluoride from water at neutral pH, *J. Water Process Eng.*, 2020, **37**, 101331, DOI: 10.1016/j.jwpe.2020.101331.

3 M. S. Kim, H. J. Choi, T. Sekino, Y. do Kim and S. H. Kim, Refractory metal oxide–doped titanate nanotubes: Synthesis

and photocatalytic activity under UV/visible light range, *Catalysts*, 2021, **11**, 987, DOI: 10.3390/catal11080987.

4 C. Zou, X. Zhao and Y. Xu, One-dimensional zirconium-doped titanate nanostructures for rapid and capacitive removal of multiple heavy metal ions from water, *Dalton Trans.*, 2018, **47**, 4909–4915, DOI: 10.1039/c8dt00405f.

5 M. Méndez-Galván, C. A. Celaya, O. A. Jaramillo-Quintero, J. Muñiz, G. Díaz and H. A. Lara-García, Tuning the band gap of M-doped titanate nanotubes (M = Fe, Co, Ni, and Cu): an experimental and theoretical study, *Nanoscale Adv.*, 2021, **3**, 1382–1391, DOI: 10.1039/d0na00932f.

6 M. Hinojosa-Reyes, R. Camposeco-Solís, F. Ruiz, N. Niño Martínez, V. Rodríguez González and M. E. Compeán-Jasso, $H_2Ti_3O_7$ Nanotubes Decorated with Silver Nanoparticles for Photocatalytic Degradation of Atenolol, *J. Nanomater.*, 2017, **2017**, 9610419, DOI: 10.1155/2017/9610419.

7 Guidelines for Drinking-water Quality Third Edition Incorporating the First And Second Addenda Volume 1 Recommendations Geneva 2008 WHO Library Cataloguing-in-Publication Data, 2008.

8 M. Bhavan, B. Shah and Z. Marg, *Bureau of Indian Standards*, 2012.

9 S. Dey and B. Giri, Fluoride Fact on Human Health and Health Problems: A Review, *Med. Clin. Rev.*, 2016, **2**, 1–6, DOI: 10.21767/2471-299x.1000011.

10 P. Chinnakoti, R. K. Vankayala, A. L. A. Chunduri, L. R. Nagappagari, S. V. Muthukonda and V. Kamisetti, Trititanate Nanotubes as highly efficient adsorbent for fluoride removal from water: Adsorption performance and uptake mechanism, *J. Environ. Chem. Eng.*, 2016, **4**, 4754–4768, DOI: 10.1016/j.jece.2016.11.007.

11 P. Loganathan, S. Vigneswaran, J. Kandasamy and R. Naidu, Defluoridation of drinking water using adsorption processes, *J. Hazardous Mater.*, 2013, **248–249**, 1–19, DOI: 10.1016/j.jhazmat.2012.12.043.

12 T. A. Saleh, Protocols for synthesis of nanomaterials, polymers, and green materials as adsorbents for water treatment technologies, *Environ. Technol. Innovation*, 2021, **24**, 101821, DOI: 10.1016/j.eti.2021.101821.

13 S. Ghosh, A. Malloum, C. A. Igwegbe, J. O. Ighalo, S. Ahmadi, M. H. Dehghani, A. Othmani, Ö. Gökkuş and N. M. Mubarak, New generation adsorbents for the removal of fluoride from water and wastewater: A review, *J. Mol. Liq.*, 2022, **346**, 118257, DOI: 10.1016/j.molliq.2021.118257.

14 A. K. Tolkou, N. Manousi, G. A. Zachariadis, I. A. Katsoyiannis and E. A. Deliyanni, Recently Developed Adsorbing Materials for Fluoride Removal from Water and Fluoride Analytical Determination Techniques: A Review, *Sustainability*, 2021, **13**, 7061, DOI: 10.3390/su13137061.

15 Y. S. Solanki, M. Agarwal, A. B. Gupta, S. Gupta and P. Shukla, Fluoride occurrences, health problems, detection, and remediation methods for drinking water: A comprehensive review, *Sci. Total Environ*, 2022, **807**, 150601, DOI: 10.1016/j.scitotenv.2021.150601.

16 T. A. Saleh, Nanomaterials: Classification, properties, and environmental toxicities, *Environ. Technol. Innovation*, 2020, **20**, 101067, DOI: 10.1016/j.eti.2020.101067.

17 S. Wan, J. Lin, W. Tao, Y. Yang, Y. Li and F. He, Enhanced Fluoride Removal from Water by Nanoporous Biochar-Supported Magnesium Oxide, *Ind. Eng. Chem. Res.*, 2019, **58**, 9988–9996, DOI: 10.1021/acs.iecr.9b01368.

18 Y. Wei, L. Wang, H. Li, W. Yan and J. Feng, Synergistic Fluoride Adsorption by Composite Adsorbents Synthesized from Different Types of Materials—A Review, *Front. Chem.*, 2022, 448, DOI: 10.3389/FCHEM.2022.900660.

19 S. S. W. Tanvir Arfin, Fluoride Removal from Water By Calcium Materials: A State-Of-The-Art Review, *Int. J. Innovative Res. Sci., Eng. Technol.*, 2015, **4**, 8090–8102, DOI: 10.15680/ijirset.2015.0409013.

20 L. K. Dhandole, H. S. Chung, J. Ryu and J. S. Jang, Vertically Aligned Titanate Nanotubes Hydrothermally Synthesized from Anodized TiO_2 Nanotube Arrays: An Efficient Adsorbent for the Repeatable Recovery of Sr Ions, *ACS Sustainable Chem. Eng.*, 2018, **6**, 16139–16150, DOI: 10.1021/acssuschemeng.8b02805.

21 N. Harsha, K. V. S. Krishna, N. K. Renuka and S. Shukla, Facile synthesis of γ-Fe_2O_3 nanoparticles integrated $H_2Ti_3O_7$ nanotubes structure as a magnetically recyclable dye-removal catalyst, *RSC Adv.*, 2015, **5**, 30354–30362, DOI: 10.1039/C5RA03722K.

22 E. K. Ylhainen, M. R. Nunes, A. J. Silvestre and O. C. Monteiro, Synthesis of titanate nanostructures using amorphous precursor material and their adsorption/photocatalytic properties, *J. Mater. Sci.*, 2012, **47**, 4305–4312, DOI: 10.1007/s10853-012-6281-x.

23 Q. Chen, G. H. Du, S. Zhang and L. M. Peng, The structure of trititanate nanotubes, *Acta Crystallogr., Sect. B: Struct. Sci., Cryst. Eng. Mater.*, 2002, **58**, 587–593, DOI: 10.1107/S0108768102009084.

24 B. C. Viana, O. P. Ferreira, A. G. Souza Filho, C. M. Rodrigues, S. G. Moraes, J. M. Filho and O. L. Alves, Decorating titanate nanotubes with CeO_2 nanoparticles, *J. Phys. Chem. C*, 2009, **113**, 20234–20239, DOI: 10.1021/jp9068043.

25 D. A. Sales, T. M. F. Marques, A. Ghosh, S. B. S. Gusmão, T. L. Vasconcelos, C. Luz-Lima, O. P. Ferreira, L. M. Hollanda, I. S. Lima, E. C. Silva-Filho, D. Dittz, A. O. Lobo and B. C. Viana, Synthesis of silver-cerium titanate nanotubes and their surface properties and antibacterial applications, *Mater. Sci. Eng., C*, 2020, **115**, 111051, DOI: 10.1016/j.msec.2020.111051.

26 S. Akel, R. Dillert, N. O. Balayeva, R. Boughaled, J. Koch, M. elAzzouzi and D. W. Bahnemann, Ag/ag2O as a co-catalyst in tiO2 photocatalysis: Effect of the co-catalyst/photocatalyst mass ratio, *Catalysts*, 2018, **8**, 647, DOI: 10.3390/catal8120647.

27 P. Quoc-Thai, T. H. Bui and L. Yong Ill, New Highly efficient electrochemical synthesis of dispersed Ag_2O particles in the vicinity of the cathode with controllable size and shape, *J. Mater. Chem. C*, 2015, **3**, 7720–7726, DOI: 10.1039/C5TC01274K.

28 D. C. de Carvalho, A. C. Oliveira, O. P. Ferreira, J. M. Filho, S. Tehuacanero-Cuapa and A. C. Oliveira, Titanate nanotubes as acid catalysts for acetalization of glycerol with

acetone: Influence of the synthesis time and the role of structure on the catalytic performance, *Chem. Eng. J.*, 2017, **313**, 1454–1467, DOI: 10.1016/j.cej.2016.11.047.

29 I. M. Iani, V. Teodoro, N. L. Marana, U. Coleto, J. R. Sambrano, A. Z. Simões, M. D. Teodoro, E. Longo, L. A. Perazolli, R. A. C. Amoresi and M. Aparecida Zaghete, Cation-exchange mediated synthesis of hydrogen and sodium titanates heterojunction: Theoretical and experimental insights toward photocatalyic mechanism, *Appl. Surf. Sci.*, 2021, **538**, 148137, DOI: 10.1016/j.apsusc.2020.148137.

30 J. V. C. do Carmo, C. L. Lima, G. Mota, A. M. S. Santos, L. N. Costa, A. Ghosh, B. C. Viana, M. Silva, J. M. Soares, S. Tehuacanero-Cuapa, R. Lang, A. C. Oliveira, E. Rodríguez-Castellón and E. Rodríguez-Aguado, Effects of the incorporation of distinct cations in titanate nanotubes on the catalytic activity in NO_x conversion, *Materials*, 2021, **14**, 2181, DOI: 10.3390/ma14092181.

31 M. S. Mahmoud, E. Ahmed, A. A. Farghali, A. H. Zaki, E. A. M. Abdelghani and N. A. M. Barakat, Influence of Mn, Cu, and Cd–doping for titanium oxide nanotubes on the photocatalytic activity toward water splitting under visible light irradiation, *Colloids Surf., A*, 2018, **554**, 100–109, DOI: 10.1016/j.colsurfa.2018.06.039.

32 P. Makuła, M. Pacia and W. Macyk, How To Correctly Determine the Band Gap Energy of Modified Semiconductor Photocatalysts Based on UV-Vis Spectra, *J. Phys. Chem. Lett.*, 2018, **9**, 6814–6817, DOI: 10.1021/acs.jpclett.8b02892.

33 V. C. Ferreira, M. R. Nunes, A. J. Silvestre and O. C. Monteiro, Synthesis and properties of Co-doped titanate nanotubes and their optical sensitization with methylene blue, *Mater. Chem. Phys.*, 2013, **142**, 355–362, DOI: 10.1016/j.matchemphys.2013.07.029.

34 V. R. Akshay, B. Arun, G. Mandal and M. Vasundhara, Visible range optical absorption, Urbach energy estimation and paramagnetic response in Cr-doped TiO_2 nanocrystals derived by a sol–gel method, *Phys. Chem. Chem. Phys.*, 2019, **21**, 12991–13004, DOI: 10.1039/c9cp01351b.

35 O. v Rambadey, A. Kumar, A. Sati and P. R. Sagdeo, Exploring the Interrelation between Urbach Energy and Dielectric Constant in Hf-Substituted $BaTiO_3$, *ACS Omega*, 2021, **6**, 32231–32238, DOI: 10.1021/acsomega.1c05057.

36 T. A. Saleh, Simultaneous adsorptive desulfurization of diesel fuel over bimetallic nanoparticles loaded on activated carbon, *J. Cleaner Prod.*, 2018, **172**, 2123–2132, DOI: 10.1016/j.jclepro.2017.11.208.

37 T. A. Saleh, Isotherm, kinetic, and thermodynamic studies on Hg(II) adsorption from aqueous solution by silica- multiwall carbon nanotubes, *Environ. Sci. Pollut. Res.*, 2015, **22**, 16721–16731, DOI: 10.1007/s11356-015-4866-z.

38 B. Choudhury, B. Borah and A. Choudhury, Extending photocatalytic activity of TiO_2 nanoparticles to visible region of illumination by doping of cerium, *Photochem. Photobiol.*, 2012, **88**, 257–264, DOI: 10.1111/j.1751-1097.2011.01064.x.

39 C. Zou, X. Zhao and Y. Xu, One-dimensional zirconium-doped titanate nanostructures for rapid and capacitive removal of multiple heavy metal ions from water, *Dalton Trans.*, 2018, **47**, 4909–4915, DOI: 10.1039/c8dt00405f.

40 A. Dhillon, T. Kumar Sharma, S. K. Soni and D. Kumar, Fluoride adsorption on a cubical ceria nanoadsorbent: Function of surface properties, *RSC Adv.*, 2016, **6**, 89198–89209, DOI: 10.1039/c6ra16962g.

41 G. Balakrishnan, R. Velavan, K. MujasamBatoo and E. H. Raslan, Microstructure, optical and photocatalytic properties of MgO nanoparticles, *Results Phys.*, 2020, **16**, 103013, DOI: 10.1016/J.RINP.2020.103013.

42 I. Langmuir, The Adsorption of Gases on Plane Surfaces of Glass, Mica and Platinum, *J. Am. Chem. Soc.*, 2002, **40**, 1361–1403, DOI: 10.1021/JA02242A004.

43 H. Freundlich, Über die Adsorption in Lösungen, *Z. Phys. Chem.*, 1907, **57U**, 385–470, DOI: 10.1515/ZPCH-1907-5723.

44 K. Babaeivelni and A. P. Khodadoust, Adsorption of fluoride onto crystalline titanium dioxide: Effect of pH, ionic strength, and co-existing ions, *J. Colloid Interface Sci.*, 2013, **394**, 419–427, DOI: 10.1016/j.jcis.2012.11.063.

45 S. George, D. Mehta and V. K. Saharan, Application of hydroxyapatite and its modified forms as adsorbents for water defluoridation: An insight into process synthesis, *Rev. Chem. Eng.*, 2020, **36**, 369–400, DOI: 10.1515/revce-2017-0101/xml.

46 W. Z. Gai and Z. Y. Deng, A comprehensive review of adsorbents for fluoride removal from water: Performance, water quality assessment and mechanism, *Environ. Sci.: Water Res. Technol.*, 2021, **7**, 1362–1386, DOI: 10.1039/d1ew00232e.